IIB 2010

Atomistic structure and energetics of interface between Mn-doped γ-Ga$_2$O$_3$ and MgAl$_2$O$_4$

Hiroyuki Hayashi · Rong Huang · Fumiyasu Oba · Tsukasa Hirayama · Isao Tanaka

Abstract The interface between an Mn-doped γ-gallium oxide (Ga$_2$O$_3$) thin film and an MgAl$_2$O$_4$ (001) substrate has been investigated using high-resolution transmission electron microscopy (HRTEM), high-angle annular dark-field scanning transmission electron microscopy (HAADF-STEM), and first-principles calculations. A high-quality Mn-doped γ-Ga$_2$O$_3$ film with a defective spinel structure has been epitaxially grown by pulsed laser deposition. The γ-Ga$_2$O$_3$ crystal shows an uniform tetragonal distortion with a tetragonality of 1.05 throughout the film thickness of 75 nm. HRTEM and HAADF-STEM observations reveal that the γ-Ga$_2$O$_3$ and MgAl$_2$O$_4$ crystals form a coherent interface without any interfacial layers or precipitates. The atomistic structure and energies are theoretically evaluated for the interfaces with two types of termination plane, i.e., Mg- and Al$_2$O$_4$-termination of MgAl$_2$O$_4$. The cation sublattice is found to be continuous for both interfaces despite the defective spinel structure of Mn-doped γ-Ga$_2$O$_3$ with some vacant cation sites. The Al$_2$O$_4$-termination shows a lower interfacial energy than the Mg-termination under most conditions of the chemical potentials. This

behavior is attributed to the energetic preference of the Mn–Al$_2$O$_4$ local configuration at the interface.

Introduction

Gallium oxide (Ga$_2$O$_3$) has attracted interests from the viewpoint of various applications, e.g., gas sensing [1], optelectronics [2, 3], and spintronics devices [4, 5]. Among the five polymorphs of Ga$_2$O$_3$ [6], the β phase with a monoclinic structure is commonly observed. On the other hand, there are a few reports on the formation of other phases through the hetero-epitaxial growth of thin films [4, 5, 7]. The examples include Mn-doped γ-Ga$_2$O$_3$ thin films with a defective spinel structure grown on α-Al$_2$O$_3$ (0001) substrates [4]. The films show ferromagnetism with a Curie temperature of above 350 K. Transmission electron microscopy (TEM) observation revealed that there are two kinds of domain, which are accompanied by [111] twin boundaries [8]. To grow epitaxial thin films of γ-Ga$_2$O$_3$ composed of a single domain, the use of MgAl$_2$O$_4$ substrates with the spinel structure can be effective. Although the lattice misfit between the γ-Ga$_2$O$_3$ ($a = 0.824$ nm) [9] and MgAl$_2$O$_4$ ($a = 0.808$ nm) [10] is estimated to be approximately 2%, we obtained epitaxial films with high crystal quality recently [11].

The hetero epitaxy is related to not only the lattice misfits between films and substrates but also interfacial structures and energies. Apart from the case that a chemical reaction occurs at the film/substrate interface, e.g., as reported in refs. [12, 13], the interfacial structure depends on the stiffness of the bonding at the interfaces and the elasticity of the two constituent crystals as well as the lattice misfits [14–16]. For instance, Ernst et al. [17] and Langjahr et al. [18] have reported the atomistic structures

H. Hayashi (✉) · F. Oba · I. Tanaka
Department of Materials Science and Engineering,
Kyoto University, Sakyo, Kyoto 606-8501, Japan
e-mail: hayashi@cms.mtl.kyoto-u.ac.jp

F. Oba
e-mail: oba@cms.mtl.kyoto-u.ac.jp

R. Huang · T. Hirayama · I. Tanaka
Nanostructures Research Laboratory, Japan Fine Ceramics
Center, Atsuta, Nagoya 456-8587, Japan

R. Huang
Key Laboratory of Polar Materials and Devices,
Ministry of Education, East China Normal University,
Shanghai 200062, China

of SrTi$_{0.5}$Zr$_{0.5}$O$_3$/SrTiO$_3$, SrZrO$_3$/SrTiO$_3$, and BaZrO$_3$/SrTiO$_3$ (100)‖(100) interfaces through high-resolution TEM (HRTEM) observations. At these interfaces with lattice misfits of 2.5, 4.9, and 7.4%, respectively, they observed misfit dislocations with periodic intervals. In contrast, such dislocations have not been clearly recognized at an SmBa$_2$Cu$_3$O$_y$/BaZrO$_3$ interface having nearly the same amount of the misfit as that at the BaZrO$_3$/SrTiO$_3$ interface [19]. The study of the SmBa$_2$Cu$_3$O$_y$/BaZrO$_3$ interface was motivated by the observation that the crystallinity of SmBa$_2$Cu$_3$O$_y$ thin films grown on MgO substrates is improved by insertion of a BaZrO$_3$ buffer layer, although the misfits between SmBa$_2$Cu$_3$O$_y$ and MgO or BaZrO$_3$ are almost the same [20, 21]. Based on the results of first-principles calculations, the effect of the BaZrO$_3$ buffer layer was attributed to the formation of the energetically preferable SmBa$_2$Cu$_3$O$_y$–BaZrO$_3$ interface associated with a good structural/chemical compatibility through the common BaO layer [19]. These reports exemplify the importance of the understanding of the detailed atomistic structure and energetics of film/substrate interfaces in the hetero epitaxy.

In this article, we report the structural analysis and interfacial energetics of a hetero-epitaxial Mn-doped γ-Ga$_2$O$_3$ thin film on an MgAl$_2$O$_4$ (001) substrate. The structure of the film/substrate interface was studied by means of X-ray reflectivity measurements and HRTEM and high-angle annular dark-field scanning transmission electron microscopy (HAADF-STEM) observations. The interfacial energy was evaluated for two types of termination plane under the relevant conditions of the chemical potentials by using first-principles calculations.

Methodology

Experimental procedures

A 75 nm-thick Mn-doped γ-Ga$_2$O$_3$ thin film was fabricated by pulsed laser deposition (PLD) using a KrF* excimer laser source ($\lambda = 248$ nm, $\tau = 25$ ns, Lambda Physik COMPex205). A laser energy of 180 mJ at the target surface, a laser frequency of 1 Hz, and a laser spot size of 6.0 mm^2 were used, which provide an optimum condition in view of the film crystallinity [11]. The target-substrate distance was set at 65 mm. An MgAl$_2$O$_4$ (001) single crystal (Shinkosha Co., Ltd.) was used for the substrate. The substrate temperature and oxygen partial pressure were kept at 673 K and 0.05 Pa during the deposition. After the deposition, the oxygen partial pressure was increased to 130 Pa and the film was cooled to room temperature. A sintered body of Ga$_2$O$_3$ doped with 5 cation% Mn was used as the PLD target, which was fabricated by sintering the mixture of commercially available high-purity powders of Ga$_2$O$_3$ and MnO$_2$ in air at 1623 K for 24 h. Powder X-ray diffraction (XRD) analysis found that the target is composed of β-Ga$_2$O$_3$ and MnGa$_2$O$_4$.

The crystal structure, crystallinity, and microstructure of the film were investigated using high-resolution five-axes XRD on a Rigaku SmartLab (Cu-Kα, 40 kV, 30 mA), and TEM and electron diffraction on a JEOL JEM3000F (300 kV). The roughness of the interface was investigated using X-ray reflectivity analysis. The direct observation of the interfacial atomic arrangements was attempted by using the HAADF-STEM technique. It has the advantage that the image contrast is roughly proportional to the square of atomic number Z and hence the assignment of atomic positions is straightforward in most cases [22, 23]. The foils for cross-sectional TEM and STEM observations of the film/substrate interface were prepared by a standard procedure which includes mechanical grinding, polishing, precision dimpling, and ion milling.

Computational procedures

Total energy calculations for Mn-doped γ-Ga$_2$O$_3$/MgAl$_2$O$_4$ interface supercells and related perfect crystal cells were conducted using the projector augmented wave (PAW) method [24] as implemented in the VASP code [25–27]. The wave functions were expanded in a plane-wave basis set with an energy cutoff of 550 eV. The generalized gradient approximation (GGA) with the Perdew–Burke–Ernzerhof (PBE) functional [28] was used. The PAW radial cutoffs are 1.5, 1.4, 1.3, 1.2, and 0.8 Å for Mg, Al, Mn, Ga, and O, respectively. Mg 3s, 3p; Al 3s, 3p; Mn 3d, 4s; Ga 3d, 4s, 4p; O 2s, 2p electrons were described as valence electrons. Spin polarization was taken into account for all calculations containing Mn. The on-site Coulomb interaction on Mn-3d orbitals was considered by the $+U$ correction (GGA $+ U$) as formulated by Dudarev et al. [29]. In this formulation, the parameters of U and J represent the on-site Coulomb interaction and the exchange interaction, respectively, and the correction depends only on the difference between U and J, $U_{\text{eff}} = U - J$. The GGA $+ U$ approach as well as the local spin density approximation $+U$ (LSDA $+ U$) has been applied to a variety of compounds containing transition metal elements, defects, and so on to describe their localized electronic states [29–34]. In this study, we used $U = 6$ eV and $J = 1$ eV corresponding to $U_{\text{eff}} = U - J = 5$ eV, which is a value in a common range for oxides involving divalent Mn [31, 32, 35]. For the systems containing Mn, ferromagnetic states were adopted. The energy differences between ferromagnetic and antiferromagnetic states were found to be negligibly small for discussing the interfacial energies: less than 0.02 eV per formula unit for Mn-doped Ga$_2$O$_3$ and relevant

reference phases, $MnGa_2O_4$ and $MnAl_2O_4$, which affects the interfacial energies only by less than 0.01 Jm^{-2}. A $2 \times 2 \times 1$ k mesh sampled with Monkhorst–Pack scheme [36] was used for the interface supercells. The supercell dimension in the direction perpendicular to the interface and all the internal coordinates were optimized until the corresponding stress component and all the atomic forces converged to less than 0.04 GPa and 0.03 eV/Å, respectively.

To construct the Mn-doped γ-Ga_2O_3/$MgAl_2O_4$ interface models, we considered $Mn_2Ga_{20}O_{32}$ as a model of Mn-doped γ-Ga_2O_3 in the defective spinel structure, which includes two cation vacant sites in the conventional unit cell of spinel. The concentration of Mn ions for the $Mn_2Ga_{20}O_{32}$ model corresponds to 9.1 cation%, which is similar to that for the Mn-doped Ga_2O_3 thin film, i.e., 7 cation% [11]. Among ~700 inequivalent configurations of two Mn ions and two cation vacant sites within this cell, we chose one structure with the lowest energy. Hereafter, this structure is denoted as "GMO". In this GMO cell, both Mn ions are located at the tetrahedral site. This trend is consistent with the results of our previous X-ray absorption near-edge structure analysis [4]. Details of the calculations for searching the lowest energy configuration will be described elsewhere [37]. For undoped γ-Ga_2O_3, we used a 40-atom supercell, which was constructed by expanding the spinel primitive cell by three times only along the c axis and removing two Ga ions. The lowest energy configuration was selected from the 14 inequivalent configurations of the two vacant Ga sites [38].

As discussed later, our HRTEM and HAADF-STEM study revealed a coherent, flat interface with (001) termination planes for both GMO and $MgAl_2O_4$ (MAO). Therefore, we considered coherent interface models, in which the lattice constant of GMO was fixed at the same value as that of MAO ($a = a_{MAO}$). The exact termination plane within the (001) planes was difficult to determine solely from the analysis of the TEM and STEM images. In the case of MAO, two types of termination, i.e., the Mg- and Al_2O_4-termination as shown in Fig. 1, can be considered. For both termination of MAO, interface models were constructed with electroneutrality conditions among the constituent ions imposed, where Mn was assumed to be divalent based on our previous X-ray absorption study [4]. We found only one structure for each termination as shown in Fig. 1. The Mg-termination model is composed of four $(Ga_2O_4)_2$, three Mn_2, and Mg_2 layers in addition to unit-cell-thick GMO and MAO layers. The Al_2O_4-termination model contains unit-cell-thick GMO and MAO layers and four $(Al_2O_4)_2$, three Mg_2, and Mn_2 layers. The supercells have two interfaces and the calculations were performed under three-dimensional periodic boundary conditions. The cell dimension in the
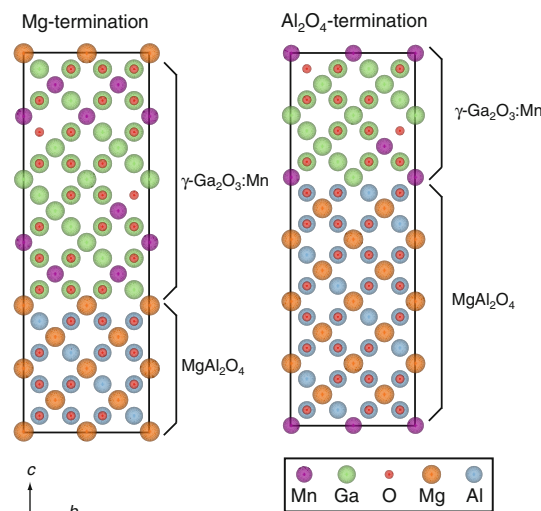

Fig. 1 *Left* Mg- and *right* Al_2O_4- terminated interface models used in the first-principles calculations [39]

direction perpendicular to the interface was optimized as well as the atomic positions.

The interfacial energy was evaluated as an excess energy per unit area relative to the relevant phases. Assuming the MnO–Ga_2O_3–MgO–Al_2O_3 pseudoquaternary system, this energy can be calculated as [40–42]

$$E_{\text{interface}} = \left(E_T - n_{\text{GMO}}\mu_{\text{GMO}} - n_{\text{MAO}}\mu_{\text{MAO}} - \sum_i n_i\mu_i\right)/2A,$$
(1)

where E_T is the total energy of a supercell containing n_{GMO} GMO and n_{MAO} MAO and two interfaces with n_i excess components ($i = MnO$, Ga_2O_3, MgO, and Al_2O_3). μ_{GMO} and μ_{MAO} denote the chemical potentials of bulk GMO and MAO, respectively, for which we use the calculated total energies per unit formula. μ_i is the chemical potential of component i, which is a variable. A is the area of the interface, and the coefficient 2 comes from the fact that the supercells contain two interfaces. The presence of the last term in the parenthesis indicates a local deviation from the stoichiometry at the interface and hence the dependence of the interfacial energy on the values of μ_i. Instead of explicitly considering the MnO–Ga_2O_3–MgO–Al_2O_3 pseudoquaternary system, we assume separate pseudobinary systems for GMO and MAO, i.e., MnO–Ga_2O_3 and MgO–Al_2O_3 for simplicity. In this case, μ_i varies within the following relations:

$$2\mu_{\text{MnO}} + 10\mu_{\text{Ga}_2\text{O}_3} = \mu_{\text{Mn}_2\text{Ga}_{20}\text{O}_{32}\text{(GMO)}},$$
(2)

$$\mu_{\text{MgO}} + \mu_{\text{Al}_2\text{O}_3} = \mu_{\text{MgAl}_2\text{O}_4\text{(MAO)}}.$$
(3)

The upper limit of μ_i with $i = Ga_2O_3$, MgO, Al_2O_3 is given by the calculated total energy of the corresponding bulk phases. Since GMO forms in the γ phase, γ-Ga_2O_3,

which is theoretically suggested to be metastable [38], is considered for i = Ga$_2$O$_3$. α-Al$_2$O$_3$ is taken for i = Al$_2$O$_3$. In the case of i = MnO, the equilibrium condition between GMO and MnGa$_2$O$_4$ spinel is used to determine the upper limit. The lower limits of μ_i are then given via Eqs. 2 and 3. For GMO, a tetragonally distorted cell with $a = a_{MAO}$ was used to compensate the energy increase associated with the distortion of the GMO lattice in the coherent interface models.

Results and discussion

Crystal structure and crystallinity of the Mn-doped γ-Ga$_2$O$_3$ film

Figure 2a shows a 2θ–θ scan around the γ-Ga$_2$O$_3$ film (004) and MgAl$_2$O$_4$ substrate (004) peaks, which are located at 42.5 and 44.8°, respectively. The film thickness was estimated to be about 75 nm through an X-ray reflection analysis as mentioned later. The narrow peak of γ-Ga$_2$O$_3$ (004) accompanied by a fringe structure demonstrates high crystal quality of the film and the uniformity in

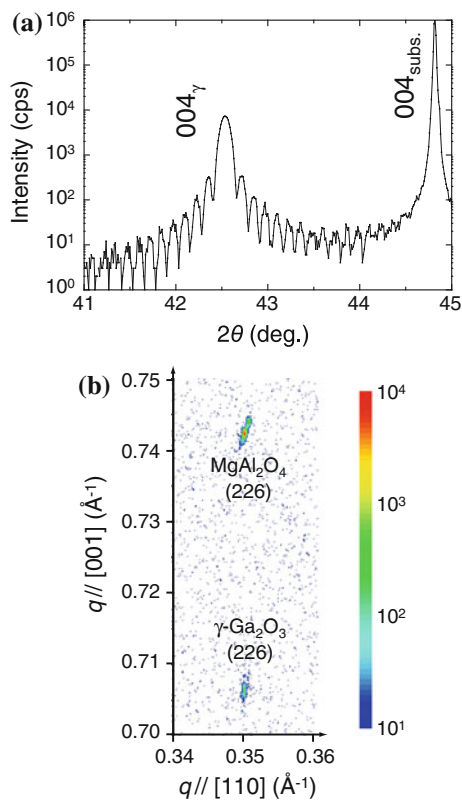**Fig. 2 a** 2θ–θ XRD profile obtained using Cu-K$_{\alpha 1}$ radiation for an Mn-doped γ-Ga$_2$O$_3$ film grown on an MgAl$_2$O$_4$ (001) substrate. **b** Reciprocal space map around the (226) diffraction spots of the film and substrate

thickness. The full width at half maximum (FWHM) of the rocking curve was found to be only 111 arcsec, which is close to that of the substrate (44 arcsec). Figure 2b shows a reciprocal space map around the (226) diffraction spots of this film and substrate. Nearly the same in-plane reciprocal coordinates of the film as that of the substrate indicates that their in-plane lattice constants are similar to each other. The in-plane lattice constant of the film is estimated to be 0.809 nm, which is indeed very close to that of MgAl$_2$O$_4$ of 0.808 nm. Meanwhile, the out-of-plane lattice constant is 0.849 nm, corresponding to a tetragonality of 1.05. The narrow diffraction spot in the in-plane direction demonstrates that the crystal is constrained by the substrate in this direction throughout the film thickness. An XRD ϕ scan revealed the single-domain structure of the film and the cube-on-cube orientation relationship with the spinel substrate (not shown). Thus, the systematic XRD analysis indicates that the Mn-doped film forms in the γ single phase and has the cube-on-cube orientation relationship with the MgAl$_2$O$_4$ substrate.

Macroscopic roughness of the film/substrate interface

The macroscopic interface roughness was investigated by an X-ray reflectivity analysis. Figure 3 presents the measured reflectivity plots compared with simulated profiles using the Parratt's equation [43]. For the simulation, the film and substrate density of 6.19 and 3.58 g/cm^3 were taken on the basis of the evaluated value from the critical angle in the reflectivity profile and the bulk value, respectively. A film thickness of 75 nm and film surface root-mean-square (RMS) roughness of 0.2 nm were derived from the Fourier transformation and fitting of the experimental profile, respectively. The interface RMS roughness was varied until the best fit was attained. In Fig. 3, the results with interface RMS roughness of 0.7 and 1.0 nm are presented. The former value yielded the best fit as shown in the inset, indicating that the interface roughness is about 0.7 nm. This value is almost the same as that for the substrate surface before the PLD of the film. Therefore, we expect that the interdiffusion at the interface is not substantial. The absence of significant interdiffusion is also supported by the TEM observations as discussed in the following section.

Structure of the interface

An HRTEM image of the interface between the Mn-doped γ-Ga$_2$O$_3$ film and MgAl$_2$O$_4$ substrate is shown in Fig. 4. The viewing direction is along the $[\bar{1}10]$ zone axis for both film and substrate. The γ-Ga$_2$O$_3$ and MgAl$_2$O$_4$ crystals are connected with each other at an atomistically flat, coherent
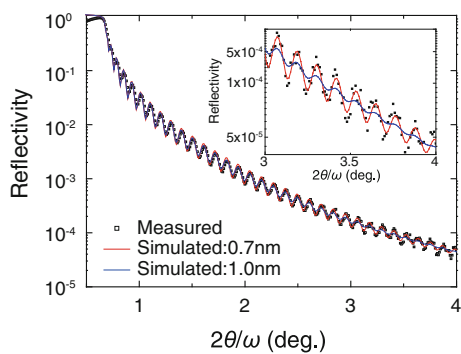
Fig. 3 Experimental and simulated X-ray reflectivity profiles of the Mn-doped γ-Ga₂O₃ film. The *inset* shows a magnified view
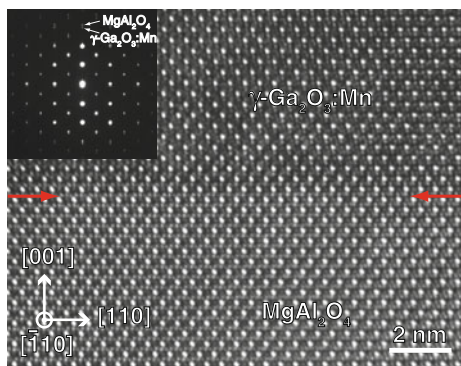

Fig. 4 Cross-sectional HRTEM image of the film/substrate interface. The zone axis is $[\overline{1}10]$ for both film and substrate. The interface is indicated by the *arrows*. The *inset* is a selected-area electron-diffraction pattern taken from a region containing both film and substrate

Fig. 5 *Upper* Cross-sectional HAADF-STEM image of the film/ substrate interface. The interface is located vertically. *Lower* Intensity profiles of the arrowed lines

Fig. 6 Relaxed atomistic structures for (*left*) Mg- and (*right*) Al₂O₄-terminated interface models [39]

interface without any interfacial layers or precipitates. The inset shows a selected-area electron-diffraction pattern obtained from an interfacial region along the $[\overline{1}10]$ zone axis for both film and substrate. The cube-on-cube orientation relationship is identified, and there are no spots other than those from γ-Ga₂O₃ and MgAl₂O₄. These features are consistent with the results of the XRD analysis. Selected-area electron-diffraction patterns from various parts of the film and substrate indicated that the lattice constants of the film are nearly constant throughout the film and that the lattice constant of the substrate near the interface is the same as that of the region far from the interface. This implies that interdiffusion between the γ-Ga₂O₃ and MgAl₂O₄ crystals is not significant.

A HAADF-STEM image and intensity line profiles are shown in Fig. 5. It is difficult to determine the exact position of the interface since the image contrast gradually changes across the interface within a region of about 1 nm. This can be attributed to the shape nonuniformity of the TEM foil across the interface made by ion-beam thinning and/or an interdiffusion occurred within the immediate
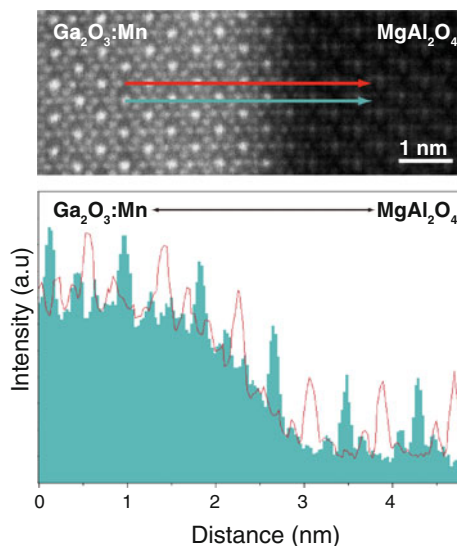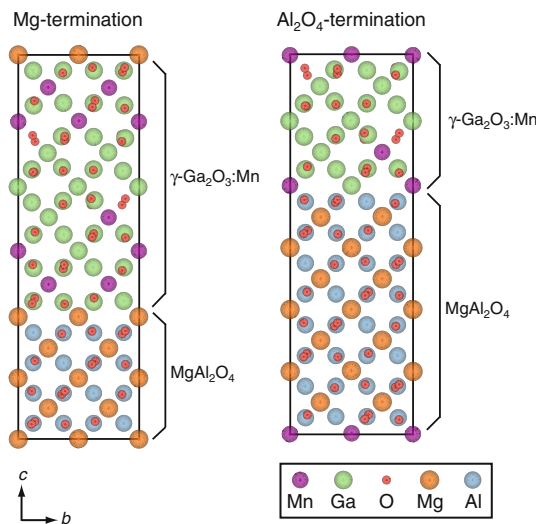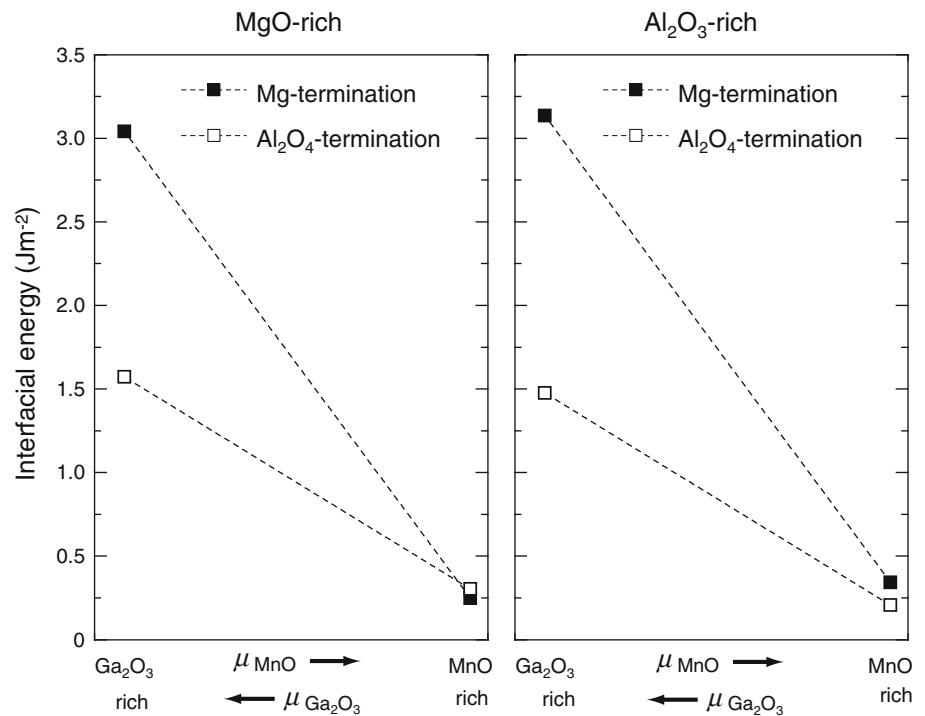
vicinity of the interface. However, it is recognized that the peaks along both lines are periodic in the interface region as in the bulk region. In addition, the image contrast is almost uniform along the interface on an atomic scale. These HAADF-STEM results together with the HRTEM image suggest the formation of an atomistically flat, coherent interface.

Energetics of the interface

Figures 6 and 7 show the calculated relaxed structures and interfacial energies for the Mg- and Al₂O₄-termination models. In both models, some of O ions are largely relaxed

Fig. 7 Interfacial energies for Mg- and Al_2O_4-termination models as a function of the chemical potentials of the MnO and Ga_2O_3 components $\left(\mu_{\mathrm{MnO}} \text{ and } \mu_{\mathrm{Ga_2O_3}}\right)$ under (*left*) the MgO-rich and (*right*) Al_2O_3-rich conditions

from the initial position in the GMO regions, which reflects the nature of GMO containing some vacant cation sites. It is noted, however, that the cations remain almost unrelaxed and they form continuous cation sublattice together with MAO across the interfaces. This feature is consistent with that found in the HRTEM and HAADF-STEM observations.

The energies of these nonstoichiometric interfaces vary with the chemical potentials of the components according to Eqs. 1–3. Concerning the dependence on μ_{MgO} and $\mu_{\mathrm{Al_2O_3}}$, the Mg- and Al_2O_4-terminated interfaces are lowered in energy under MgO- and Al_2O_3-rich conditions, respectively, as shown in the left and right panels of Fig. 7. Since μ_{MgO} and $\mu_{\mathrm{Al_2O_3}}$ vary within only a small range of 0.4 eV via Eq. 3, the changes in interfacial energy are small. As for the μ_{MnO} $\left(\mu_{\mathrm{Ga_2O_3}}\right)$ dependence, both interface models have MnO-rich composition compared with GMO, and, therefore, are favored in energy under high values of μ_{MnO} (low values of $\mu_{\mathrm{Ga_2O_3}}$). The Mg-termination model shows a larger dependence on μ_{MnO} $\left(\mu_{\mathrm{Ga_2O_3}}\right)$ than the Al_2O_4-termination model because of the larger number of the MnO component. Under both MgO- and Al_2O_3-rich conditions, the energy of the Al_2O_4-termination model is lower for most values of μ_{MnO} $\left(\mu_{\mathrm{Ga_2O_3}}\right)$. This trend can be considered from the viewpoint of the stability of local configurations at the interfaces. The Mg-termination model has an Mg–Ga_2O_4 configuration at the interface. The Al_2O_4-termination model has Mn–Al_2O_4 and Ga–Al_2O_4 configurations. In the following discussion, only the contribution of the Mn–Al_2O_4 configuration is considered

because the number of the Mn–Al_2O_4 configuration per unit interfacial area is three times larger than that of the Ga–Al_2O_4 configuration. The stability of these local configurations can be assessed on the basis of the formation energies of $MgGa_2O_4$ and $MnAl_2O_4$ normal spinels. Therefore, the formation energies of undistorted cubic $MgGa_2O_4$ and $MnAl_2O_4$ crystals and those with tetragonal distortion of $a = a_{\mathrm{MAO}}$ were calculated with reference to MgO, γ-Ga_2O_3, MnO, and γ-Al_2O_3. For γ-Al_2O_3, the same vacant cation site configuration as that in the undoped γ-Ga_2O_3 model was considered. The results are listed in the Table 1. $MnAl_2O_4$ is lower in formation energy than $MgGa_2O_4$ in the undistorted cubic case. This tendency is enhanced by the tetragonal distortion, which can be partly attributed to the equilibrium lattice constant of $MnAl_2O_4$ closer to that of MAO and hence the smaller strain. Therefore, the Mn–Al_2O_4 local configuration is suggested to be energetically more favorable than the Mg–Ga_2O_4 configuration at the interface.

Table 1 Formation energies of $MgGa_2O_4$ and $MnAl_2O_4$ with reference to MgO, γ-Ga_2O_3, MnO, and γ-Al_2O_3

Cell shapes	Formation energy (eV/f. u.)	
	$MgGa_2O_4$	$MnAl_2O_4$
Cubic	−1.45	−1.54
Tetragonal	−1.33	−1.51

Two types of cell in shape, i.e., undistorted cubic and tetragonally distorted cells, are considered

Conclusions

The atomistic structure and energy of the Mn-doped γ-Ga_2O_3/$MgAl_2O_4$ interface have been investigated using HRTEM, HAADF-STEM, and first-principles calculations. The epitaxially grown Mn-doped γ-Ga_2O_3 is tetragonally distorted throughout the film thickness of 75 nm. No interfacial layers or precipitates have been observed at the interface. A coherent atomistic configuration of the interface is indicated by the continuous intensity profiles in the HAADF-STEM image. In the interfacial atomistic structures obtained using the first-principles calculations, the cation sublattice is continuous for the two types of termination at the interface, i.e., Mg- and Al_2O_4-termination. This is remarkable considering the defective spinel structure of Mn-doped γ-Ga_2O_3 with some vacant cation sites. The Al_2O_4-termination is lower in interfacial energy than the Mg-termination under most conditions of the chemical potentials, which is attributed to the energetic preference of the Mn–Al_2O_4 local configuration at the interface.

References

1. Ogita M, Saika N, Nakanishi Y, Hatanaka Y (1999) Appl Surf Sci 142:188
2. Víllora EG, Yamaga M, Inoue T, Yabasi S, Masui Y, Sugawara T, Fukuda T (2002) Jpn J Appl Phys Part 2 41:L622
3. Oshima T, Okuno T, Fujita S (2007) Jpn J Appl Phys Part 1 46:7217
4. Hayashi H, Huang R, Ikeno H, Oba F, Yoshioka S, Tanaka I, Sonoda S (2006) Appl Phys Lett 89:181903
5. Kaneko K, Nomura T, Kakeya I, Fujita S (2009) Appl Phys Express 2:075501
6. Roy R, Hill VG, Osborn EF (1952) J Am Chem Soc 74:719
7. Matsuzaki K, Hiramatsu H, Nomura K, Yanagi H, Kamiya T, Hirano M, Hosono H (2006) Thin Solid Films 496:37
8. Huang R, Hayashi H, Oba F, Tanaka I (2007) J Appl Phys 101:063526
9. Zinkevich M, Morales FM, Nitsche H, Ahrens M, Rühle M, Aldinger F (2004) Z Metallkd 95:756
10. Yamanaka T, Takeuchi Y (1983) Z Kristallogr 165:65
11. Hayashi H, Huang R, Oba F, Hirayama T, Tanaka I (2011) J Mater Res (in press)
12. Liu R, Bohannan EW, Switzer JA, Oba F, Ernst F (2003) Appl Phys Lett 83:1944
13. Oba F, Ernst F, Yu YS, Liu R, Kothari M, Switzer JA (2005) J Am Ceram Soc 88:253
14. Ikuhara Y, Pirouz P (1993) Ultramicroscopy 52:421
15. Ernst F, Raj R, Rühle M (1999) Z Metallkd 90:961
16. Ernst F (2002) Philos Mag A 82:2677
17. Ernst F, Rečnik A, Langjahr PA, Nellist PD, Rühle M (1998) Acta Mater 47:183
18. Langjahr PA, Lange FF, Wagner T, Rühle M (1998) Acta Mater 46:773
19. Oba F, Sugawara Y, Hasegawa K, Izumi T, Shiohara Y, Hirayama T, Yamamoto T, Ikuhara Y (2004) J Appl Phys 95:2309
20. Hasegawa K, Hobara N, Nakamura Y, Izumi T, Shiohara Y (2002) J Jpn Inst Met 66:320
21. Hasegawa K, Shibata J, Izumi T, Shiohara Y, Sugawara Y, Hirayama T, Oba F, Ikuhara Y (2003) Physica C 392:835
22. Pennycook SJ, Jesson DE (1991) Ultramicroscopy 37:14
23. Buban JP, Matsunaga K, Chen J, Shibata N, Ching WY, Yamamoto T, Ikuhara Y (2006) Science 311:212
24. Blöchl PE (1994) Phys Rev B 50:17953
25. Kresse G, Hafner J (1993) Phys Rev B 48:13115
26. Kresse G, Furthmuller J (1996) Phys Rev B 54:11169
27. Kresse G, Joubert D (1999) Phys Rev B 59:1758
28. Perdew JP, Burke K, Ernzerhof M (1996) Phys Rev Lett 77:3865
29. Dudarev SL, Botton GA, Savrasov SY, Humphreys CJ, Sutton AP (1998) Phys Rev B 57:1505
30. Anisimov VI, Zaanen J, Andersen OK (1991) Phys Rev B 44:943
31. Posternak M, Baldereschi A, Massidda S, Marzari N (2002) Phys Rev B 65:184422
32. Franchini C, Bayer V, Podloucky R, Paier J, Kresse G (2005) Phys Rev B 72:045132
33. Choi M, Oba F, Tanaka I (2009) Phys Rev Lett 103:185502
34. Kumagai Y, Oba F, Yamada I, Azuma M, Tanaka I (2009) Phys Rev B 80:085120
35. Tran F, Blaha P, Schwarz K, Novák P (2006) Phys Rev B 74:155108
36. Monkhorst HJ, Pack JD (1976) Phys Rev B 13:5188
37. Hayashi H, Huang R, Oba F, Seko A, Tanaka I (unpublished)
38. Yoshioka S, Hayashi H, Kuwabara A, Oba F, Matsunaga K, Tanaka I (2007) J Phys Condens Matter 19:346211
39. Momma K, Izumi F (2008) J Appl Crystallogr 41:653
40. Benedek R, Alavi A, Seidman DN, Yang LH, Muller DA, Woodward C (2000) Phys Rev Lett 84:3362
41. Zhang W, Smith JR (2000) Phys Rev B 61:16883
42. Zhang W, Smith JR (2000) Phys Rev Lett 85:3225
43. Parratt LG (1954) Phys Rev 95:359